JACS
JOURNAL OF THE AMERICAN CHEMICAL SOCIETY
Article
pubs.acs.org/JACS

# Spectroscopic Evidence for a $3d^{10}$ Ground State Electronic Configuration and Ligand Field Inversion in $[Cu(CF_3)_4]^{1-}$

Richard C. Walroth,[†] James T. Lukens,[†] Samantha N. MacMillan,[†] Kenneth D. Finkelstein,[‡] and Kyle M. Lancaster*[,†]

[†]Department of Chemistry and Chemical Biology, Baker Laboratory, Cornell University, Ithaca, New York 14853, United States
[‡]Cornell High Energy Synchrotron Source, Wilson Laboratory, Cornell University, Ithaca, New York 14853, United States

Supporting Information

**ABSTRACT:** The contested electronic structure of $[Cu(CF_3)_4]^{1-}$ is investigated with UV/visible/near IR spectroscopy, Cu K-edge X-ray absorption spectroscopy, and 1s2p resonant inelastic X-ray scattering. These data, supported by density functional theory, multiplet theory, and multireference calculations, support a ground state electronic configuration in which the lowest unoccupied orbital is of predominantly trifluoromethyl character. The consensus $3d^{10}$ configuration features an inverted ligand field in which all five metal-localized molecular orbitals are located at lower energy relative to the trifluoromethyl-centered $\sigma$ orbitals.

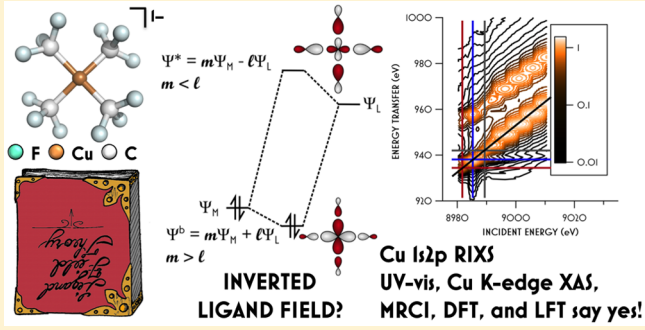


## INTRODUCTION

Trifluoromethyl ($CF_3$) substituents profoundly influence the properties of organic molecules[1] and transition metal complexes.[2] Medicinal chemists have recognized the value of the $CF_3$ group for adding advantageous drug properties including increased physiological longevity, facile blood−brain barrier penetration, and enhanced protein−substrate binding affinities.[1] Consequently, the development of chemical reactions that install $CF_3$ groups on organic frameworks is a major research goal.[3] The desire for late-stage, selective functionalization has fostered the rapid growth of transition-metal-mediated trifluoromethylation reactions and has increased interest in preparing discrete, fluorinated organometallic complexes.[3c,4] For example, Hartwig and co-workers[5] reported the synthesis of $Cu(phen)(CF_3)$ (**1**; phen = 1,10-phenanthroline; Figure 1). This stable compound is readily synthesized from inexpensive starting materials and trifluoromethylates a wide range of iodoarenes with high functional group tolerance under mild reaction conditions.

In a recent report, Grushin[6] and co-workers described an improved synthesis of the highly unusual, formally $Cu^{III}$ complex ion $[Cu(CF_3)_4]^{1-}$ (**2**; Figure 1), which is traditionally prepared with the toxic and explosive $Cd(CF_3)_2$ as a transmetalation reagent. The authors showed that salts of **2** can be easily prepared from CuCl and $TMSCF_3$/KF (TMS = trimethylsilyl) in air, in a high-yielding, one-step reaction. These species are air-stable, and in all cases the complex ion adopts a $D_{2d}$, flattened tetrahedral geometry. To date, there have been no reports of **2** exhibiting standard nucleophilic trifluoromethylation reactivity, although the dearth of studies may be due in part to the former lack of synthetically accessible methods for the preparation of **2**. Detailed mechanistic studies by Grushin and co-workers indicate that **2** is an off-path, catalytically incompetent species in the Cu-mediated oxidative trifluoromethylation of aryl boronic acids.[7]

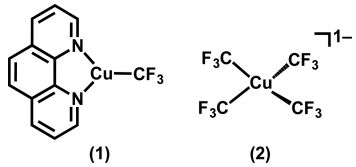


**Figure 1.** $Cu(phen)(CF_3)$ (**1**; phen =1,10-phenanthroline) is a versatile trifluoromethylating reagent. To date, trifluoromethylation by $[Cu(CF_3)_4]^{1-}$ (**2**) has not been demonstrated.

The disputed[8] electronic structure of **2** postulated by Snyder[9] suggests that **2** should be considered a source of *electrophilic*, not nucleophilic, $CF_3$. Although **2** is formally considered a $d^8$ $Cu^{III}$ species, Snyder proposed that it is better described as *physically* $d^{10}$ $Cu^{I}$ based on a computational study that gave a partial charge on Cu of 0.71 and d-orbital populations of 9.7 or 9.4, depending on the level of theory used. With a $Cu^{I}$ configuration, charge balance necessitates that **2** be coordinated by three $CF_3^-$ ligands and one $CF_3^+$ ligand. Owing to resonance, in a valence bond picture this would best be described as delocalized $CF_3^+$ character over the molecule, or, after the manner of Jørgensen,[10] $Cu^{I}$ surrounded by a $(CF_3)_4^{2-}$ coordination sphere. Snyder's argument thus describes **2** as featuring an "inverted" ligand field[11] in which the lowest

**Received:** October 23, 2015
**Published:** February 4, 2016





DOI: 10.1021/jacs.5b10819
J. Am. Chem. Soc. 2016, 138, 1922−1931

unoccupied molecular orbital (LUMO) exhibits dominantly ligand orbital admixture, contrary to the classical ligand field in which the frontier orbitals are dominated by metal d-orbital admixture (Figure 2). This point was later strongly supported

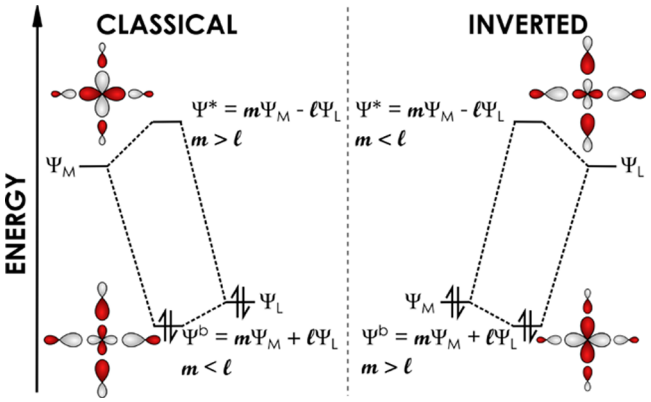


**Figure 2.** In a classical Werner-type ligand field, the antibonding orbital Ψ* is dominated by metal d-orbital character. An inverted ligand field arises when Ψ* has predominantly ligand orbital character.

by Mealli.[12] Although such an inversion has been noted in electronic structure calculations of the $LaFe_4P_{12}$ skutterudite,[13] and hinted at in several additional studies,[14] an experimentally verified molecular example remains elusive.

Assignment of oxidation states based on density functional theory (DFT)-derived partial charges remains controversial,[8] and theoretical studies have found that partial charges on metal centers do not vary with overall charge.[11b] Moreover, this particular compound may elude conventional description because of the counterintuitive electronic and structural effects imparted by $CF_3$.[3c] Although theorists have studied **2** for several years,[8,9,11b,15] few experimental electronic structural characterizations have been offered in support of either ground state configuration. Herein we report spectroscopic data and calculations that support $d^{10}$ as the ground state electronic configuration of **2**.

## EXPERIMENTAL SECTION

**General Considerations.** Crystalline samples of **2-PPN** [PPN = bis(triphenylphosphine)iminium] and **2-PPh$_4$** [$PPh_4$ = tetraphenylphosphonium] were provided by V. Grushin, and were prepared according to a published procedure.[16] UV/visible/near IR (UV/vis/NIR) spectra of solutions of **2** salts dissolved in dichloromethane (dried using a JC Meyer solvent system) were measured on a Cary 5000 spectrophotometer. $CuF_2$ was purchased from Sigma-Aldrich and used without further purification.

**X-ray Spectroscopy.** Samples for X-ray spectroscopy were prepared as solid mixtures in boron nitride. All mixtures contained 5% by mass Cu. The mixtures were finely ground in an agate mortar, pressed into 1 mm aluminum spacers, and sealed with 38 $\mu$m Kapton tape.

Cu K-edge X-ray absorption spectroscopy (XAS) spectra of **2-PPN** and **2-PPh$_4$** were measured in transmission mode with $N_2$-filled ionization chambers at beamline 7−3 of the Stanford Synchrotron Radiation Lightsource (SSRL) under ring conditions of 3 GeV and 500 mA. Incident X-ray radiation was monochromated by using a double Si(220) crystal monochromator. Incident energy was calibrated by using Cu foil as an internal calibrant, with the energy of the first inflection point set to 8980.3 eV. Samples were maintained at 10 K in an Oxford liquid He cryostat. Spectra were measured from 8900 to 9300 eV. Four scans were measured and averaged with the EXAFSPAK[17] software package. No spectral changes due to photodamage were observed after four scans. Background subtraction was achieved by fitting a polynomial to the pre-edge region and subtracting this polynomial from the entire spectrum. Spectra were normalized by fitting a flattened polynomial to the postedge and normalizing the edge jump at 9000 eV to 1.0.

1s2p resonant inelastic X-ray scattering (RIXS) of **2-PPN** and $CuF_2$ were collected at the Cornell High Energy Synchrotron Source (CHESS) C1 bend magnet beamline under ring conditions of 5.3 GeV and 100 mA. Incident X-ray radiation was monochromated using a Rh mirror and sagittal focus double Si(220) monochromator and calibrated as described above for experiments at SSRL. X-ray emission was collected, monochromated, and focused with five spherically bent Si(444) crystals in a Rowland circle geometry by using the CHESS dual array valence emission spectrometer (DAVES), which has been described elsewhere.[18] X-ray emission was collected with a Pilatus 100 K area detector (Dectris). Two regions of interest (ROIs) were selected in order to correct X-ray emission intensity (I): the first (ROI1) contained >95% of the X-ray emission; the second (ROI2) comprised a region centered on the first ROI but with twice the width and height. The larger ROI was used to determine the average background counts per pixel, which was used to estimate the total background per point on the scan.

$$I_{\text{corrected}} = I_{\text{ROI1}} - \text{Area}_{\text{ROI1}}\left(\frac{I_{\text{ROI2}} - I_{\text{ROI1}}}{\text{Area}_{\text{ROI2}} - \text{Area}_{\text{ROI1}}}\right) \quad (1)$$

X-ray emission was corrected for incident photon flux by dividing counts from an $N_2$-filled ionization chamber placed just upstream of the sample.

Emission energy was calibrated by measuring the K$\alpha_1$ and K$\alpha_2$ lines of Cu foil and setting corresponding points on the DAVES Rowland geometry to 8046.3 and 8026.7 eV, respectively. Photodamage was not detected in fewer than six scans, so a maximum of six scans were collected for each spot. Constant 9100 eV incident energy scans of K$\alpha$ emission were measured at each new spot on a sample for normalization. Samples were maintained at ca. 150 K by using an Oxford $N_2$ cold stream focused at the beam spot. The temperature at the spot was measured using a thermocouple.

RIXS planes were collected by scanning the emission domain at constant incident energy. For each compound, 20 incident energies were chosen along the pre-edge and rising edge regions This strategy is demonstrated for **2-PPN** in Figure S5 and Figure S6. Point densities were varied to focus collection time on specific regions along the Cu K-edge. The collection strategies are included as Supporting Information. Emission intensity was normalized by collecting emission spectra at a constant 9100 eV incident energy and setting the peak maximum of the K$\alpha_1$ peak to 1.

Data were processed with Igor 6.37. Emission spectra were converted to the energy transfer domain, and individual spectra were combined to create incident energy (IE), energy transfer (ET), and intensity tabulated as *x*, *y*, and *z* scatter data. Vertical traces were generated directly by converting emission spectra to the ET domain. Horizontal traces were generated by plotting average intensity values within 0.4 eV of the desired constant energy transfer while ensuring unique values per incident energy.

**Calculations.** DFT, time-dependent DFT (TDDFT), DFT-restricted open-shell configuration interaction with single excitations (DFT-ROCIS), and spectroscopy-oriented configuration interaction (SORCI) calculations were performed with version 3.03 of the ORCA[19] software package. All spectra were calculated from crystallographic coordinates of the **2** complex ion in **2-PPN**.[16] Calculations did not employ molecular symmetry. Irreducible representations are assigned to orbitals by inspection using the symmetry operations in a $D_{2d}$ character table. Single-point energies were calculated by using BP86,[20] B3LYP,[21] M06,[22] $\omega$B97,[23] $\omega$B97X,[23] $\omega$B97X-D3,[23] LC-BLYP,[24] and CAM-B3LYP[24] functionals. Calculations with hybrid functionals used the RIJCOSX algorithm to speed the calculation of Hartree−Fock exchange.[25] The CP(PPP)[26] basis set was used for Cu with a special integration accuracy (ORCA Grid7). The scalar relativistically recontracted def2-TZVP(-f)-ZORA[27] basis set with


DOI: 10.1021/jacs.5b10819
J. Am. Chem. Soc. 2016, 138, 1922−1931

ORCA Grid4 was used for all other atoms. Calculations included the zeroth-order regular approximation (ZORA) for relativistic effects[28] as implemented by van Wüllen.[29] Solvation was modeled with COSMO[30] in an infinite dielectric.

Electronic absorption and Cu K-edge XAS spectra were calculated by using TDDFT.[31] Spectral predictions used the $\omega$B97X functional. The CP(PPP) basis set was used for Cu with an integration accuracy of 7. The def2-TZVP-ZORA basis set was used for all other atoms. Solvation was again modeled by using COSMO in an infinite dielectric.

DFT-ROCIS is described elsewhere[32] and was used to calculate Cu $L_{2,3}$-edge XAS spectra with the $\omega$B97X-calculated electronic structure. Transitions were restricted to those involving the three Cu 2p orbitals as donors. Unoccupied orbitals involved in the most intense Cu K-pre-edge absorptions were chosen as ROCIS acceptor orbitals. $Cu^{III}$ $L_{2,3}$-edge XAS was simulated independently with the TT-Multiplets code[33] as implemented in the CTM4XAS graphical user interface.[34]

Multireference character in the ground state of **2** was assessed with SORCI[35] calculations. SORCI was performed on a complete active space (CAS) for **2** comprising 16 electrons and 10 orbitals [CAS(16,10)]. The CP(PPP) basis set was used on Cu, and def2-TZVP(-f)-ZORA was used on all other atoms. The ZORA relativistic correction was used in all SORCI calculations. As described elsewhere,[35] individual selection was used to ease the computational burden. The size of the first-order interacting space was reduced with a threshold: $T_{sel} = 10^{-6}$ $E_h$. A further approximation involved reducing the reference space through another selection: all initial references that contributed less than a second threshold ($T_{pre} = 10^{-5}$) to the zeroth-order states were rejected from the reference space. Starting orbitals were taken from restricted Kohn–Sham orbitals generated via the aforementioned $\omega$B97X/def2-TZVP(-f)-ZORA calculation.

## RESULTS AND DISCUSSION

**Ligand Field Analysis.** The $D_{2d}$ geometry of **2** has been used to argue against the $d^{10}$ configuration,[8] but regardless of its configuration, **2** is a 16-electron complex. A $\sigma$-only angular overlap analysis[36] comparing *inverted* $D_{4h}$ and $T_d$ ligand field diagrams reveals that $D_{4h}$ remains the favored geometry despite the $d^{10}$ configuration (Figure 3). Additionally, in the $d^8$ limit, **2** should exhibit a moderately absorptive d-d band ($\varepsilon$ ca. 100 $M^{-1}$ $cm^{-1}$) corresponding to $^1A \rightarrow {}^1E$ excitation. No absorption bands are observed in vis/NIR spectra of solutions of **2-PPN** between 30 000 and 6250 $cm^{-1}$ (Figure S1). Intense bands due to charge-transfer absorptions ($\varepsilon$ > 20 000 $M^{-1}$ $cm^{-1}$) are found in the UV spectrum to energies greater than 30 000 $cm^{-1}$ (Figure 4). The burying of the $^1A \rightarrow {}^1E$ d-d band beneath the charge-transfer features implies an unrealistically high value for crystal field splitting in a four-coordinate Cu complex.

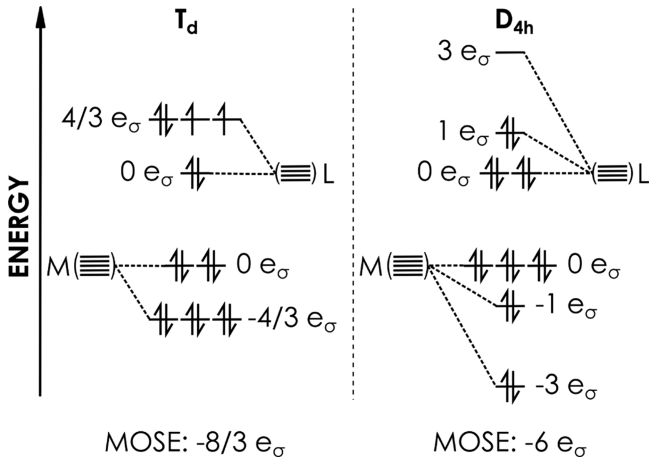


**Figure 3.** $\sigma$-Only molecular orbital (MO) diagrams generated via the angular overlap method for 16-electron complexes with inverted ligand fields at the $T_d$ and $D_{4h}$ geometry limits. Total MO stabilization energy (MOSE) determinations show that despite the $d^{10}$ configuration, $D_{4h}$ geometry is favored in an inverted ligand field picture.

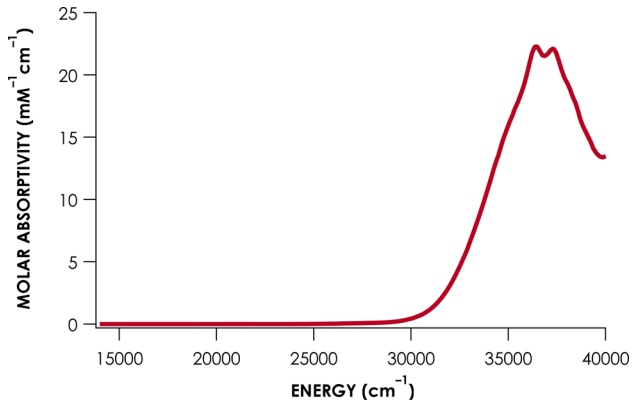


**Figure 4.** UV/visible spectrum of **2-PPN** [PPN = bis(triphenylphosphine)iminium] recorded in dichloromethane.

**Cu K-edge XAS.** Cu K-edge XAS data for **2-PPN** were obtained to complement the UV/vis/NIR data. Cu K-edge XAS data were also obtained for **2-$PPh_4$**—the identity of the counterion has no effect on peak energies (Figure S3). K-edge XAS has become a standard means of measuring physical oxidation states in first-row transition metal compounds.[37] For example, Solomon and co-workers[38] comprehensively demonstrated that the pre-edge features in the K-edge XAS spectra of formally $Cu^{III}$ compounds appear at approximately 8981 eV and thus are ca. 2 eV to higher energy relative to $Cu^{II}$ compounds, for which pre-edges are typically observed near 8979 eV. This shift to higher energy exhibited by $Cu^{III}$ complexes is attributed to an increase in effective nuclear charge commensurate with higher oxidation state. The increase in the effective charge lowers the core electrons to a deeper binding energy, which in turn gives rise to higher-energy pre-edges and rising edges.

The Cu K-edge XAS spectrum for **2-PPN** is feature-rich (Figure 5). Multiple features are resolved from the rising edge, the inflection point of which occurs at 8997.2 eV. We assigned the most intense absorption at 8985.6 as the dipole-allowed Cu 1s → 4p transition. This feature is isoenergetic with the 1s → 4p transition in $D_{4h}$, $Cu^{II}$ $[CuCl_4](nmph)_2$ (**3-nmph**; nmph =

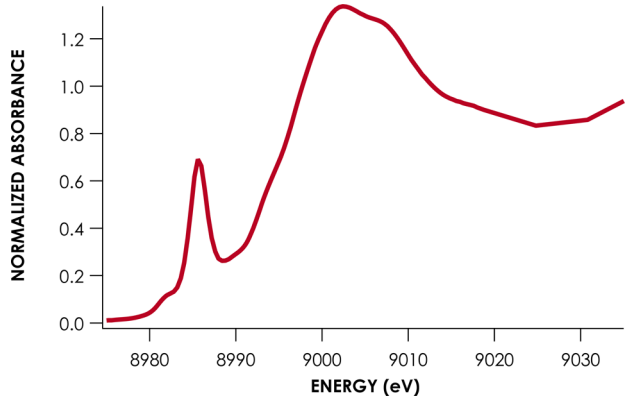


**Figure 5.** Transmission-mode Cu K-edge X-ray absorption spectroscopy (XAS) spectrum of solid **2-PPN**.



DOI: 10.1021/jacs.5b10819
J. Am. Chem. Soc. 2016, 138, 1922–1931

methyl(2-phenylethyl)ammonium) and is 1.7 eV lower in energy compared to analogous transitions in the $Cu^{III}$ species discussed by Solomon and co-workers.[38] The 8985.6 eV feature is also within the energy range reported for four-coordinate $Cu^{I}$ complexes.[39] A considerably weaker feature is found to lower energy at 8982.0 eV. By convention, the observation of a feature at this energy supports a $Cu^{III}$ configuration; in these cases the transition represents a $1s^23d^8 \rightarrow 1s^13d^9$ excitation. However, recent reinterpretation of Cu K-edge XAS data by Wieghardt and co-workers[40] has challenged the diagnostic use of pre-edge energy as a metric of oxidation state in Cu systems. DFT as well as ab initio multireference calculations for a number of formally $Cu^{III}$ complexes have revealed that the $d^8$ electronic configuration makes insignificant contributions to the ground states of these molecules. These authors[40] suggest that in these cases, the pre-edge excitations are best described as *formally* metal-to-ligand charge transfer (MLCT), owing to the fact that the acceptor orbitals are dominated by ligand admixture. Contributions from Cu 3d and 4p confer allowedness to these excitations via electronic quadrupole and dipole contributions, respectively.[41] Moreover, weak K-edge XAS pre-edge features have been observed and assigned in "closed-shell" $d^{10}$ $Cu^{I}$ systems.[42] In these systems—such as $[Cu(bpy)_2]^+$ (bpy = 2,2′-bipyridine)—that bear ligands with unoccupied valence molecular orbitals (MOs) lying energetically beneath Cu 4p, such *formal* metal-to-ligand charge transfer (MLCT) transitions have been observed near 8981 eV. The energies of these transitions can be rationally modulated by tuning bpy $\pi$-system energetics, and the transitions are well modeled using TDDFT. It should be noted that, as distinct from an optical MLCT, the transition moments giving rise to such features are small, and the transition densities are effectively metal-localized due to the highly contracted nature of the donor metal 1s orbital. Such transitions mirror the pre-edge excitations in ligand K-edge XAS, where although the transitions may be formally described as ligand-to-metal charge transfer (LMCT), the contracted ligand 1s orbitals give rise to small transition moments where the transition densities are localized to the ligand atoms.[43] For clarity, we will distinguish such charge transfer features as XAS-MLCT/XAS-LMCT, as distinct from optical MLCT and LMCT.

In the case of **2**, Snyder's[9] postulated $Cu^{I}$ configuration necessitates a "$CF_3^+$" LUMO, which could give rise to a quadrupole-allowed pre-edge XAS-MLCT feature due to a $1s^23d^{10}L \rightarrow 1s^13d^{10}L^{\bullet}$ excitation in which L represents a $CF_3$ $\sigma$-based MO. Alternatively, the 8982 eV feature could be assigned to $1s^23d^{10}4p^0 \rightarrow 1s^13d^{10}4p^1$. Excitation to a $1s^13d^{10}4s^1$ configuration is forbidden. Both allowed possibilities are considered below.

**1s2p RIXS.** The photophysics of Cu K-edge XAS can be exploited to assign the 8982 eV feature exhibited by **2-PPN**. Excited states with $1s^1$ configurations rapidly (ca. $10^{15}$ $s^{-1}$) deactivate through X-ray emission (Figure 6). The deactivation pathways of highest probability involve $\Delta l = \pm 1$, 2p → 1s transitions called K$\alpha$ emissions. In the $d^8$ $Cu^{III}$ limit (Figure 6a), the final electronic configuration is $1s^22p^53d^9$. This configuration will give rise to multiple nondegenerate electronic states. Two states, analogous to $P_{1/2}$ and $P_{3/2}$ terms in the free ion limit, arise with a ca. 20 eV splitting owing to Cu 2p spin–orbit coupling (SOC).[44] These states exhibit additional splitting due to 2p-3d electron–electron exchange. In the $d^{10}$ limit (Figure 6b,c), K$\alpha$ emission from the $1s^13d^{10}L^{\bullet}$ or $1s^13d^{10}4p^1$ intermediate states generate either $1s^22p^53d^{10}L^{\bullet}$ or

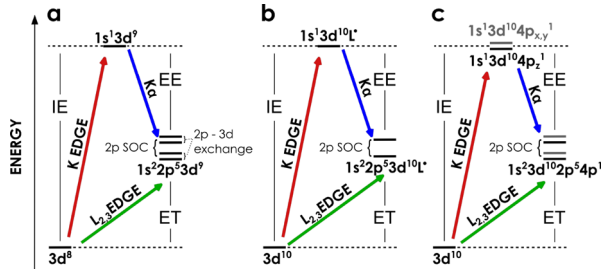


**Figure 6.** Qualitative energy diagrams depicting intermediate and final electronic states accessed by the lowest-energy Cu K-pre-edge excitations in $d^8$ (a) and $d^{10}$ (b,c) formulations for **2**. The incident energy (IE) causes excitation from Cu 1s, giving rise to Cu K-edge XAS features. Subsequent X-ray emission at emission energy (EE) gives final configurations that match those accessed with Cu $L_{2,3}$-edge XAS. The difference (IE − EE) gives energy transfer (ET), the values of which will match $L_{2,3}$-edge XAS excitations. In both limits, the final $2p^5$ configurations will split into two states due to ca. 20 eV Cu 2p spin–orbit coupling (SOC). In the $d^8$ limit, 2p-3d exchange will cause additional splitting to give four final states. In the $d^{10}$ limit where the initial excitation is to a ligand-centered d-orbital (b), only two final states will be apparent. In case (c), where the lowest excitation populates p-orbitals split by the $D_{2d}$ ligand field, four RIXS features will appear.

$1s^23d^{10}2p^54p^1$ configurations, the states of which are split by Cu 2p SOC. In the latter case (Figure 6c), ligand field splitting of Cu 4p gives two possible excitation/deactivation paths: a path involving excitation to Cu $4p_z$, and, to higher energy, excitation to Cu $4p_{x,y}$. The exchange interaction between the Cu 2p and either $CF_3$-localized or 4p-localized electrons is expected to be vanishingly small owing to the large separation between radial probability maxima.

These final states are the same as those accessed with Cu $L_{2,3}$ ($2p_{1/2}/2p_{3/2}$ → valence/continuum) XAS.[45] However, Cu $L_{2,3}$-edge XAS is an experimentally demanding soft X-ray technique that requires ultrahigh vacuum conditions and in which samples are rapidly photodamaged.[46] Moreover, ambiguities can arise in the assignment of side bands, which may be due to either electronic structure or X-ray scattering events including extended X-ray absorption fine structure. Electronic processes in Cu $L_{2,3}$ XAS can alternatively be probed with 1s2p RIXS, which is considered an effective facsimile of L-edge XAS.[44,46b,47] RIXS is a hard X-ray, three-dimensional spectroscopy that presents X-ray emission intensity as a function of incident X-ray photon energy (IE) and emitted photon energy (EE). The EE axis is converted by convention into energy transfer ET (ET = IE − EE). 1s2p RIXS displays energetic separations owing to 2p SOC, and side bands due to electronic exchange will also be resolved if the incident energy bandwidth is sufficiently narrow.

Different "slices" of the resulting plane provide complementary information about the electronic structure of the compound under study. Plotted diagonal slices give high-energy-resolution fluorescence-detected (HERFD) XAS spectra. HERFD-XAS reduces uncertainty broadening, thereby producing XAS spectra with considerably narrower line widths.[48] Plotting slices at constant IE shows the X-ray emission transitions that deactivate intermediate states populated by 1s excitations. For example, ET features with energies that match the $L_{2,3}$-edge (2p → 3d) XAS maxima are seen in the 1s2p RIXS analysis of $CuF_2$ at IE resonant with Cu 1s → 3d excitation at 8978.0 eV (Figure S2).[45]


DOI: 10.1021/jacs.5b10819
J. Am. Chem. Soc. 2016, 138, 1922–1931

The 1s2p RIXS plane of **2-PPN** obtained with DAVES at CHESS is shown in Figure 7 (bottom left). The majority of the

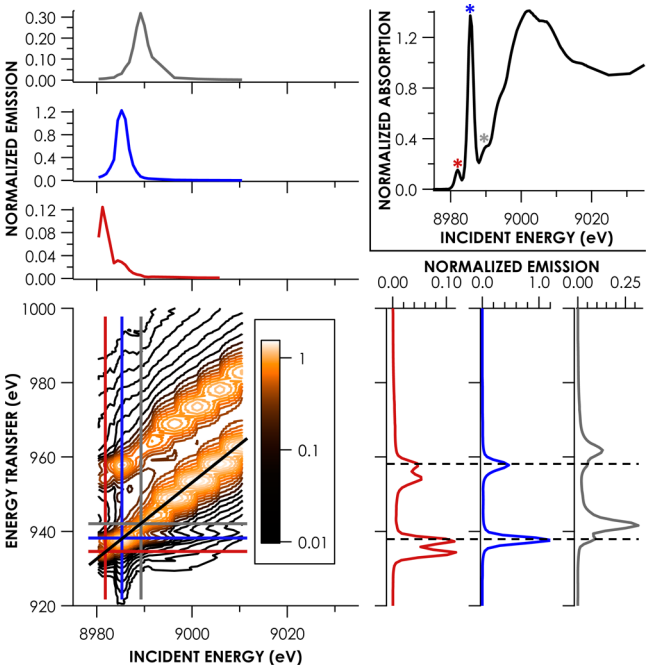


**Figure 7.** 1s2p resonant inelastic X-ray scattering (RIXS) plane of solid **2-PPN** is plotted in the lower left. Constant ET slices with colors corresponding to solid horizontal lines on the RIXS plane are plotted in the upper left. Constant IE slices with colors corresponding to the vertical solid lines on the RIXS plane are plotted in the lower right. Points on the Cu K-edge XAS spectrum corresponding to the IE slices are marked with color-coded asterisks. A diagonal slice corresponding to the black solid line gives the HERFD XAS spectrum of **2-PPN**, which is plotted in the upper right.

X-ray emission intensity is found along parallel diagonals, which represent final $2p^5$ states split by Cu 2p SOC amounting to 20.0 eV. Plotting RIXS intensity along these diagonals gives the HERFD-XAS spectra of **2-PPN** (Figure 7, top right), in which pre-edge and rising-edge features are resolved with full-widths at half-maximum (fwhm) of 1.5 eV, which is 2-fold narrower than the width in the corresponding transmission-mode spectrum (Figure S4). Emission at IEs resonant with the three observed pre-edge XAS features are plotted in the lower right of Figure 7. Excitation at 8982.0 eV (red vertical slice) gives rise to an emission spectrum (Figure 7, bottom right) with energies determined via the fitting of pseudo-Voigt peaks. On-diagonal features appear at 934.2 and 954.2 eV. Off-diagonal bands appear at 937.4 and 958.0 eV. The fwhm for these features are ca. 2 eV.

Cramer and co-workers[44] have shown that 2p-3d and 3d-3d exchange give rise to well-resolved, ca. 5 eV off-diagonal splitting in high-spin $Ni^{II}$ 1s2p RIXS; low-spin $Ni^{II}$ lacks 3d-3d exchange splitting. However, neither interaction is the origin of the side bands in the 1s2p RIXS spectrum of **2-PPN**. Another origin would be 3d-3d exchange. However, salts of **2** are diamagnetic,[16] necessitating either a closed-shell or singlet diradical ground state configuration. In the case of either a classical or inverted ligand field, the highest MO with Cu d-character is nondegenerate. In the diradical case, 3d-3d exchange would energetically favor a triplet ground state over a singlet. Moreover, the ground state would have orbital degeneracy and be subject to a Jahn–Teller distortion. While the latter consequence need not necessarily manifest in observable geometric distortion, the diamagnetism of **2** rules out open-shell configurations. Consequently, no side bands will arise due to 3d-3d exchange in the RIXS of **2-PPN**. While additional features are observed at 937.4 and 958.0 eV, it should be noted that these bands are isoenergetic with the emission features arising from 8985.6 eV IE (blue vertical slice). Plotting constant ET at 937.4 and 958.0 eV (denoted by the dashed lines in Figure 7) gives peak maxima at 8985.6 eV IE (see Figure 7, top left blue spectrum). Thus, these features do not originate from excitation at 8982.0 eV, but rather arise from the decay of the higher-energy intermediate state with configuration $1s^14p^1$ that is adventitiously accessed because IE bandwidth exceeds that of the 8982 eV pre-edge feature. This causes excitation into the state corresponding to the next XAS feature at 8985.6 eV. Plotting emission intensity at ET values that would be consistent with 2p-3d exchange (vide infra) as a function of IE shows that all emission intensity arises due to 8985.6 eV IE and that none of this intensity originates from 8982 eV IE. The lack of residual off-diagonal intensity arising from 8982 eV IE is consistent with vanishingly small Cu 2p-3d exchange, although distinction between excitation to $1s^13d^{10}L^{\bullet}$ versus $1s^13d^{10}4p^1$ remains at this point ambiguous. Regardless, the 1s2p RIXS spectrum for **2-PPN** is consistent with a ground state electronic configuration approaching the $d^{10}$ limit.

We assign the 934.2 and 954.2 eV features as the $L_3$-and $L_2$-edge maxima, respectively, for **2-PPN**. The energies of these peaks are both ca. 2 eV higher than the corresponding values found during L-edge XAS studies of $Cu^{III}$ species by Solomon and co-workers.[49] Together with the high energy found for the first pre-edge band in the Cu K-edge XAS spectrum, this shift suggests a LUMO with an energy placed above the Cu 3d manifold, also consistent with the inverted ligand field framework.

**DFT Calculations.** Single-point DFT calculations were carried out with ORCA[19] to produce an MO description of the ground state electronic configuration of **2**. Solomon and co-workers have noted that calculations of Cu covalency are highly functional-dependent. These authors benchmarked several functionals in calculations of the electronic structure of the thoroughly characterized $D_{4h}$ $Cu^{II}$ complex ion $CuCl_4^{2-}$ (**3**), for which a self-consistent, experimental value of 0.62 ± 0.02 electrons has been determined for the spin population of the singly occupied MO (Cu $3d_{x^2-y^2}$).[50] These authors observed that BP86 returns an inverted ligand field for **3**, which is an electronic structure that is inconsistent with spectroscopic characterization.

We carried out single-point calculations of **3** with various density functionals while keeping constant the use of the CP(PPP) basis set on Cu and the segmented all-electron relativistically recontracted def2-TZVP(-f)-ZORA basis set on Cl (Table 1). Our test set of functionals included several modern range-separated functionals.[23] Löwdin spin population analyses were used to estimate Cu–Cl covalency.[51] Whereas BP86 returns an inverted ligand field for **3**, B3LYP, M06 and the range-separated functionals produce a bonding scheme that is more consistent with experiment. We noted that ωB97X and its dispersion-corrected ωB97X-D3 variant gave splendid agreement with the experimental value, yielding values of 0.61 and 0.60 electrons, respectively. Cognizant of the functional sensitivity of Cu covalency, we employed BP86,


DOI: 10.1021/jacs.5b10819
J. Am. Chem. Soc. 2016, 138, 1922–1931

Table 1. Calibration Calculations of Cu Covalency in 3[a]

| functional | % Cu 3d[b] |
|---|---|
| BP86 | 0.47 |
| B3LYP | 0.56 |
| M06 | 0.55 |
| ωB97X | 0.61 |
| ωB97X-D3 | 0.60 |
| CAM-B3LYP | 0.59 |
| LC-BLYP | 0.54 |
| experiment[c] | 0.62 ± 0.02 |

[a]Calculations used the def2-TZVP(-f)-ZORA basis for Cl and CP(PPP) for Cu. [b]Spin population on Cu. [c]See ref 49.

B3LYP, and ωB97X in DFT calculations of the electronic structure of **2**.

Frontier MO diagrams for **2** produced at the BP86/def2-TZVP(-f)-ZORA, B3LYP/def2-TZVP(-f)-ZORA, and ωB97X/def2-TZVP(-f)-ZORA levels of theory are shown in Figure 8 and orbital energies and coefficients are given in Table 2. In accord with Snyder's[9] earlier finding, the $b_2$-symmetry $\sigma^*$ LUMO ($2b_2$) is dominated by $CF_3$ $\sigma$ character in all cases. These results are generated using crystallographic coordinates for **2** in **2-PPN**, and geometry optimizations using either BP86 or B3LYP do not influence the outcome (see Tables S1 and S2). The Cu $3d_{xy}$ contributions to $2b_2$ range from 29% (BP86) to 33% (ωB97X). $CF_3$ $\sigma$ MOs contribute 64% (BP86) to 59% (ωB97X). Residual contributions to $2b_2$ are from Cu $4p_z$. The three highest occupied MOs calculated via B3LYP and ωB97X are principally of $CF_3$ parentage, and to deeper binding energy are found the five fully occupied Cu 3d orbitals with an ordering that is the inverse of classical $T_d$ ligand field-splitting. The BP86 results largely preserve the ligand field inversion, although the ligand-centered $a_1$ orbital is calculated to lower energy than the metal-centered $a_1$.

**Spectral Simulations via TDDFT and ROCIS.** All employed density functionals produce a consensus electronic structure in which the conventional ordering of metal-centered and ligand-centered MOs is inverted. The aforementioned electronic structure calculations using crystallographic coordinates were used as starting points for spectral predictions. Results of these calculations are essentially identical, so only spectral calculations employing ωB97X will be discussed; the results from the BP86 and B3LYP calculations are included in the SI.

Table 2. Molecular Orbital Energies and Coefficients[a] for 2[b]

| BP86 | | | | | |
|---|---|---|---|---|---|
| orbital | energy (eV) | % Cu 3d | % Cu 4s | % Cu 4p | % $CF_3$ σ |
| $2b_2$ (LUMO) | −3.3 | 29.8 | 0.0 | 4.5 (*z*) | 63.8 |
| 2e (2-fold degenerate) | −6.6 | 4.8 | 0.0 | 6.4 (*x*) | 76.8 |
| | | | | 6.4 (*y*) | |
| $2a_1$ | −7.4 | 4.8 | 10.5 | 0.0 | 26.7 |
| 1e (2-fold degenerate) | −8.2 | 59.5 | | 0.2 (*x*) | 9.3 |
| | | | | 0.2 (*y*) | |
| $1b_1$ | −8.5 | 88.7 | 0.0 | 0.0 | 8.9 |
| $1a_1$ | −8.9 | 88.7 | 3.6 | 0.0 | 53.5 |
| $1b_2$ | −9.4 | 89.6 | 0.0 | 0.0 | 37.9 |
| B3LYP | | | | | |
| orbital | energy (eV) | % Cu 3d | % Cu 4s | % Cu 4p | % $CF_3$ σ |
| $2b_2$ (LUMO) | −2.8 | 32.0 | 0.0 | 4.5 (*z*) | 61.5 |
| 2e (2-fold degenerate) | −7.7 | 1.9 | 0.0 | 6.7 (*x*) | 78.7 |
| | | | | 6.7 (*y*) | |
| $2a_1$ | −9.0 | 35.9 | 12.7 | 0.0 | 46.4 |
| 1e (2-fold degenerate) | −10.3 | 90.2 | 0.0 | 0.0 | 8.5 |
| $1a_1$ | −10.7 | 62.0 | 1.1 | 0.0 | 31.6 |
| $1b_1$ | −10.7 | 82.8 | 0.1 | 0.0 | 15.9 |
| $1b_2$ | −10.8 | 56.6 | 0.0 | 0.0 | 38.6 |
| ωB97X | | | | | |
| orbital | energy (eV) | % Cu 3d | % Cu 4s | % Cu 4p | % $CF_3$ σ |
| $2b_2$ (LUMO) | −0.7 | 34.1 | 0.0 | 4.7 (*z*) | 58.9 |
| 2e (2-fold degenerate) | −10.4 | 1.2 | 0.0 | 6.9 (*x*) | 78.8 |
| | | | | 6.9 (*y*) | |
| $2a_1$ | −12.1 | 27.9 | 12.6 | 0.0 | 53.3 |
| 1e (2-fold degenerate) | −13.5 | 86.9 | 0.0 | 0.0 | 12.4 |
| | | | | 0.0 | |
| $1b_2$ | −13.8 | 52.2 | 0.0 | 0.0 | 42.6 |
| $1a_1$ | −13.9 | 66.4 | 0.5 | 0.0 | 28.5 |
| $1b_1$ | −13.9 | 80.1 | 0.0 | 0.0 | 19.1 |

[a]Summed Löwdin orbital coefficients. [b]Calculations on crystallographic coordinates using the CP(PPP) basis set on Cu and def2-TZVP(-f)-ZORA on all other atoms.

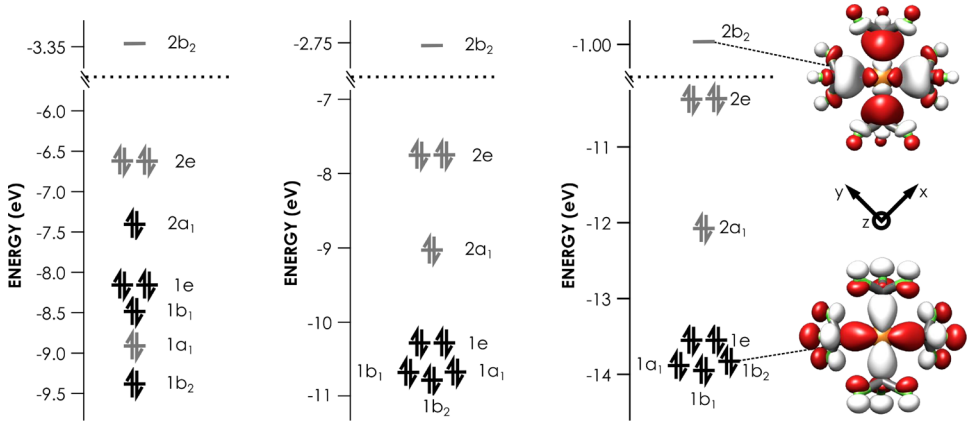


**Figure 8.** Frontier MO diagrams of **2** at the BP86/def2-TZVP(-f)-ZORA, B3LYP/def2-TZVP(-f)-ZORA, and ωB97X/def2-TZVP(-f)-ZORA levels of theory. The CP(PPP) basis set was used on Cu in all calculations. Cu-localized MOs are shown in black, and ligand-localized orbitals are gray. The $b_2$ bonding and antibonding MOs from the ωB97X calculation are plotted at an isolevel of 0.03 au.



DOI: 10.1021/jacs.5b10819
J. Am. Chem. Soc. 2016, 138, 1922−1931

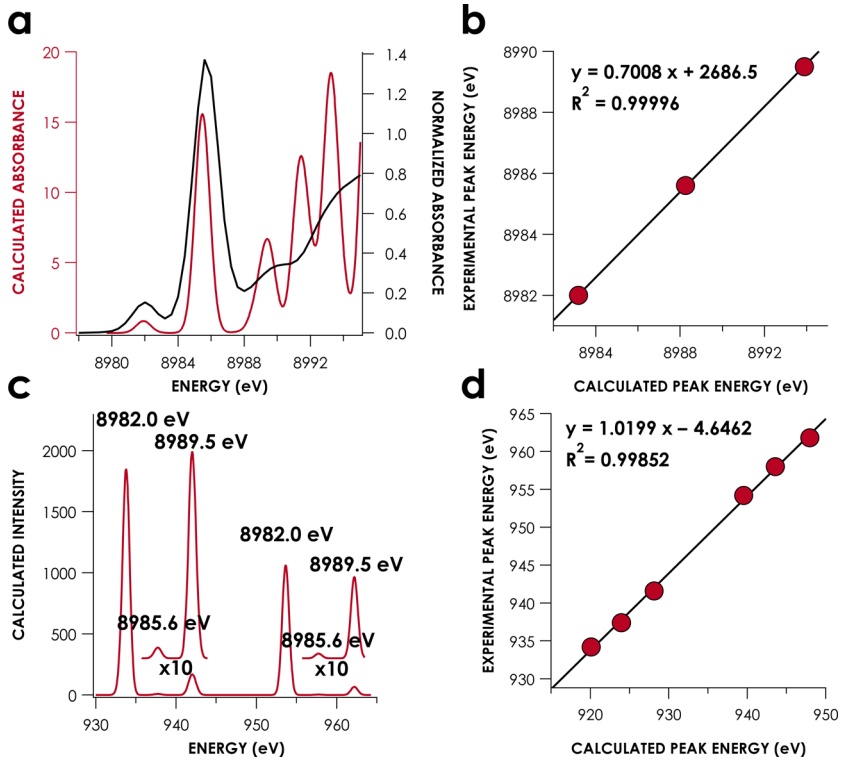


**Figure 9.** (a) High-energy-resolution fluorescence-detected (HERFD) XAS spectrum of **2-PPN** (black) overlaid on the energy-corrected time-dependent density functional theory calculated spectrum (red). (b) Calculated transition energies were empirically adjusted according to the strong correlation to experimental peak energies. (c) Calculated, energy-corrected 1s2p RIXS ET features of **2-PPN** arising at IEs corresponding to the three lowest energy pre-edge XAS features. (d) Calculated RIXS ET peak energies correlate strongly with experimental values. All spectral calculations were initiated from the $\omega$B97X/def2-TZVP(-f)-ZORA solution.

The lowest-lying spin-allowed excited state calculated via TDDFT was found at 37 089.4 $cm^{-1}$, which agreed with the UV/vis/NIR results, and it arises due to charge-transfer excitations (Figures S10). The dominant contributing excitations to the ca. 35 000 $cm^{-1}$ absorption feature are 2-fold degenerate, $^1A_1 \rightarrow {}^1E$ MLCT transitions. No d-d bands were predicted. TDDFT calculations of the Cu K-edge XAS results accurately reproduced the relative energy separations among the first three pre-edge bands resolved in the HERFD data with a correlation coefficient of $R^2 = 1.0$ (Figure 9a,b). The 8982 eV pre-edge feature is predicted by TDDFT calculations to be Cu 1s $\rightarrow$ 2$b_2$ $\sigma^*(CF_3)$. Under $D_{2d}$ symmetry, 4$p_z$ will mix with this MO, in accord with the relatively high intensity of this pre-edge transition. The feature at 8985.6 eV arises due to Cu 1s $\rightarrow$ 4$p_z$ excitations. The feature at 8989.5 eV comprises numerous excitations. Major contributions arise due to excitations from Cu 1s to $CF_3$ $\pi^*$ orbitals with small (ca. 5%) Cu 3d admixture.

The TDDFT-calculated Cu K-edge spectra were used to guide DFT-ROCIS[32] calculations of Cu $L_{2,3}$ XAS findings to model the 1s2p RIXS data. For the DFT-ROCIS calculations, the Cu 2p orbitals were chosen as donors, and three valence MOs participating in the 8982.0, 8985.6, and 8989.5 eV excitations were chosen as acceptor orbitals. The calculated energies of the three pairs of Cu 2p SOC-split features correlated with $R^2$ = 1.0 to experiment (Figure 9c,d). Importantly, no side-bands due to 2p-3d exchange were observed in the calculated RIXS features arising due to the 8982.0 eV IE excitation.

Relative $L_{2,3}$ peak areas are well-reproduced by the DFT-ROCIS procedure for all functionals investigated.[52] The ratios of peak areas in $L_{2,3}$-edge XAS are conventionally expressed in terms of the branching ratio, which is given as $I(L_3)/[I(L_3) + I(L_2)]$. Thole and Van der Laan[53] have shown that this branching ratio is linearly related to valence SOC. In the present case, this is the magnitude of Cu 3d SOC and, thus, the branching ratio reflects the relative contributions of Cu 3d and $CF_3$ $\sigma^*$ to the orbital probed by emission with 8982 eV resonant excitation. The branching ratio resulting from DFT-ROCIS calculations is 0.64 for all functionals, in good agreement with the experimental value of 0.69. This branching ratio is consistent with an acceptor orbital involved in the 8982 eV excitation for which Cu 3d makes a minor contribution (vide infra).

Intensities for RIXS ET bands corresponding to 8985.6 and 8989.5 eV IE were severely underestimated with this method. However, this outcome is readily explained: these features arise in the RIXS slices due to 2p $\rightarrow$ 1s demotions and are formally $|\Delta l| = 1$, thus obeying atomic selection rules. The DFT-ROCIS method calculates these bands as $L_{2,3}$ excitations. Because the 8985 eV band is Cu 2p $\rightarrow$ Cu 4p with a $\Delta l$ of 0, the corresponding RIXS features are formally forbidden and thus of low intensity. The large disparity in intensities between the RIXS features arising from 8982 and 8985.6 eV excitation supports assignment of the 8982 eV excitation as XAS-MLCT from Cu 1s to 2$b_2$ $\sigma^*(CF_3)$. The band at 8989.5 eV contains contributions from $CF_3$ $\pi^*$ orbitals with ca. 5% 3d contributions. The corresponding $L_{2,3}$ excitation will be weak due to this small d-contribution.

**X-ray Spectral Simulations via Multiplet Theory.** Multiplet calculations[33] were carried out to evaluate the magnitude of Cu 2p-3d exchange splitting that would be apparent when accessing $2p^53d^9$ states with 1s2p RIXS in the


DOI: 10.1021/jacs.5b10819
J. Am. Chem. Soc. 2016, 138, 1922–1931

$Cu^{III}$ $d^8$ limit. An $O_h$ crystal field was chosen with $\Delta_o$ estimated at 0.5 eV from DFT. The value of $F_{dd}$ was set to 0 to reflect diminished 3d-3d exchange due to the closed-shell ground state configuration of **2**. Values of 2p-3d exchange were scaled from 100% ($d^8$ limit) to 0% ($d^{10}$ limit) by concomitantly varying reduction factors of the Slater $F_{pd}$ and $G_{pd}$ integrals from 1.0 to 0.0. A pseudo-Voigt broadening was chosen with a total fwhm value of 2.0 eV comprising equal Gaussian and Lorentzian contributions. This value was chosen based on experimental line widths. The results of these calculations are plotted in Figure 10.

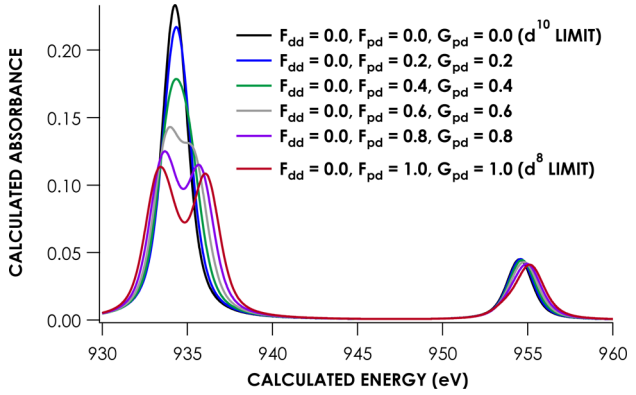


**Figure 10.** TT-multiplet simulations of Cu $L_{2,3}$-edge XAS data from the $d^{10}$ to $d^8$ limits in 2p-3d exchange. An octahedral crystal field with a $\Delta_o$ of 0.5 eV was used for all calculated spectra. 3d-3d exchange was abolished by setting $F_{dd}$ to 0.0. 2p-3d exchange was modulated by varying $F_{pd}$ and $G_{pd}$ together from 0.0 ($d^{10}$ limit) to 1.0 ($d^8$ limit). Pseudo-Voigt line broadening with 2 eV full-widths at half-maximum (fwhm) was applied to each spectrum.

The multiplet calculations show that 2p-3d exchange manifests in the $d^8$ limit as a 2.4 eV split of the $L_3$ band into two features of approximately equal intensity. At reduction factors of 40% and lower (approaching $d^{10}$), these features coalesce to a single band. The calculation with 40% reduction of the 2p-3d integrals gives an $L_3$ peak at 934.2 eV and an $L_2$ peak at 954.5 eV in excellent agreement with experimental values. However, the relative peak areas do not agree with experiment for any value of integral reduction.

A second set of multiplet calculations was performed, this time holding $F_{dd}$ at 0.0, $F_{pd}$ at 0.4, and $G_{pd}$ at 0.4. Valence SOC (the 3d SOC) was scaled from 0% to 100%, and the resulting spectra are plotted in Figure 11. Shown in the inset of Figure 11 is the linear relationship between the branching ratio and the percent valence SOC. Interpolation of the experimental value of the branching ratio (0.69) found for **2** shows that the data are best modeled with the valence SOC reduced to 15%, in further accord with a largely $CF_3$-centered LUMO.

**SORCI Calculations.** SORCI calculations were carried out to evaluate multireference character in the ground state of **2**. SORCI calculations were initiated from a CAS containing the 16 valence electrons in $\sigma$ orbitals. The eight orbitals harboring these electrons, as well as the LUMO and LUMO+1, were chosen for the CAS for a final CAS(16,10) reference. SORCI calculations were initiated with orbitals from the $\omega$B97X/def2-TZVP(-f)-ZORA DFT calculation. Ten singlet, triplet, and quintet states were calculated, and the chosen CAS captured >90% of the reference configurations. Both variations of the SORCI procedure revealed that the ground state of **2** is

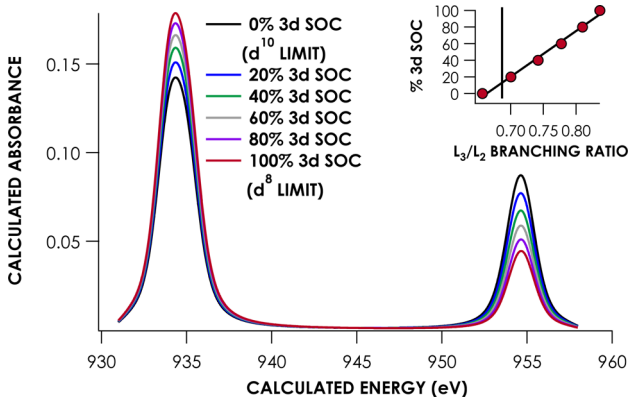


**Figure 11.** TT-multiplet simulations of Cu $L_{2,3}$-edge XAS data from the $d^{10}$ to $d^8$ limits in valence spin−orbit coupling (SOC). An octahedral crystal field with a $\Delta_o$ of 0.5 eV was used for all calculated spectra. 3d-3d exchange was abolished by setting $F_{dd}$ to 0.0. 2p-3d exchange was held at 40% reduction with $F_{pd}$ and $G_{pd}$ values set to 0.4. The value of valence (3d) SOC was scaled from 0% to 100%. A pseudo-Voigt line broadening with 2 eV fwhm was applied to each spectrum. The inset shows the linear correlation between valence SOC and the $L_3/L_2$ branching ratio defined as $I(L_3)/[I(L_3) + I(L_2)]$. A vertical line marks the branching ratio of **2**, corresponding to 15% 3d SOC.

effectively single-reference and dominated by the closed-shell configuration determined with DFT (Table S7). The reference weight of this configuration was 0.86. Singlet diradical configurations amount to less than 5% of the ground state references. The lowest-lying triplet and quintet states are calculated at 3.2 and 8.9 eV above the ground state, respectively. The inverted ligand field MO scheme for **2** was conserved after the configuration interaction (CI) treatment (Figure S13). The UV/vis spectrum generated by using the ten states of each spin multiplicity is provided in Figure S14. This spectrum is in good agreement with the experimental UV/vis/NIR data and again features a lack of d-d transitions.

**Extension to Additional Cu-$CF_3$ Complexes.** The aforementioned analyses indicate that DFT calculations at the $\omega$B97X/def2-TZVP(-f)-ZORA level successfully model the electronic structure of **2**. These calculations were extended to **1** as well as to Cu(bpy)$(CF_3)_3$ (**4**) and Cu(edtc)$(CF_3)_2$ (**5**; edtc = diethyldithiocarbamate; Figure 12). Similar to **2**, **4** and **5** have to date been described as formally $d^8$ $Cu^{III}$ species. However, ligand field inversion resurfaces, with the LUMOs of both molecules exhibiting electronic vacancy of $CF_3$-centered MOs. The five Cu-localized MOs are filled, giving a $d^{10}$ configuration. By contrast, the LUMO of **1** is phen $\pi^*$. All $CF_3$-localized MOs are filled, and in light of these comparisons, the reactivity of **1** as a source of nucleophilic "$CF_3^-$" is readily apparent, whereas the presence of a formally "$CF_3^+$" species on **2**, **4**, and **5** suggests that these molecules could serve as unique, metal-based sources of electrophilic $CF_3$. Such reactivity studies are under way in our laboratory.

## SUMMARY AND OUTLOOK

The assembled spectroscopic data and supporting calculations establish a limiting $d^{10}$ configuration for **2**. This result necessitates an inversion of the MO ordering from the classical, Werner-type ligand field picture. Formally, the coordination sphere of **2** should exhibit electrophilic "$CF_3^+$" character. Our results showcase the utility of 1s2p RIXS for the assignment of


DOI: 10.1021/jacs.5b10819
J. Am. Chem. Soc. 2016, 138, 1922−1931

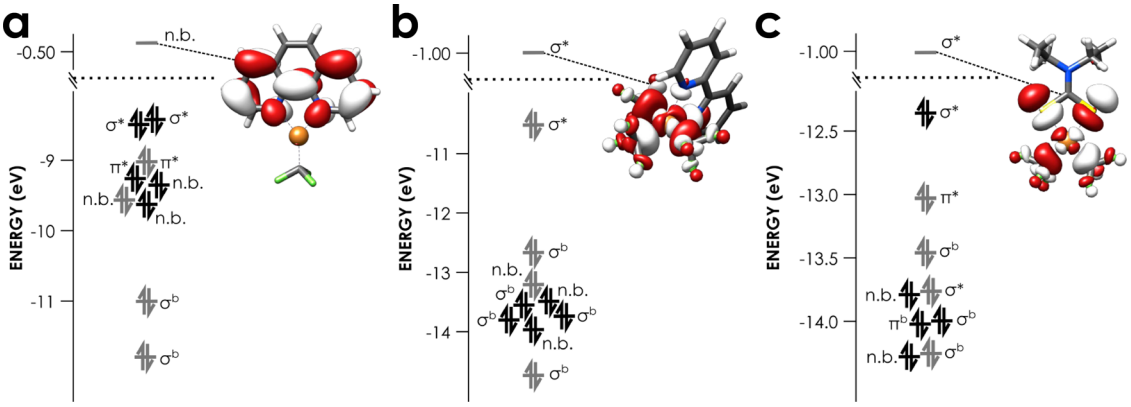


**Figure 12.** Frontier MO diagrams of **1** (a), **4** (b), and **5** (c) at the ωB97X/def2-TZVP(-f)-ZORA level of theory. Cu-localized MOs are shown in black, and ligand-localized orbitals are gray. Lowest unoccupied molecular orbitals are plotted at an isolevel of 0.03 au.

XAS pre-edge features, and they show that XAS-MLCT features can arise at energies once considered diagnostic of $Cu^{III}$. The ROCIS-DFT method predicts 1s2p RIXS ET features with relative energy separations that scale to splendid agreement with experiment. Extending our experimentally validated calculations to related formally $Cu^{III}$ compounds shows that the $d^8$ description is, in several cases, inconsistent with experimentally validated electronic structure calculations. These results, combined with those of the aforementioned studies by Wieghardt and co-workers,[40] indicate that reevaluation of the electronic structures of high-valent Cu species—particularly purported $Cu^{IV}$ species including $Cs_2CuF_6$[54] and recently reported Cu corrolato monocations[55]—is merited. Such studies, as well as investigations into both the physical origin and the reactivity consequences of the ligand field inversion exhibited by **2** and related compounds are forthcoming.

## ■ ASSOCIATED CONTENT

### Supporting Information

The Supporting Information is available free of charge on the ACS Publications website at DOI: 10.1021/jacs.5b10819.

NIR data for **2-PPN**, Cu K-edge XAS data for **2-PPh$_4$**, 1s2p RIXS data for $CuF_2$, 1s2p RIXS data collection strategy, representative ORCA input files, ORCA input coordinates, DFT orbital plots for **2**, DFT orbital energies and admixture coefficients following geometry optimization of **2**, DFT orbital energies and admixture coefficients for **1**, **4**, and **5**, TDDFT calculated UV/vis/NIR spectra of **2**, SORCI results, and SORCI-calculated UV/vis/NIR spectrum of **2**. (PDF)

## ■ AUTHOR INFORMATION


### Corresponding Author

*kml236@cornell.edu


### Notes

The authors declare no competing financial interest.

## ■ ACKNOWLEDGMENTS

We thank Vladimir Grushin for supplying the salts of the title complex ion, and we thank Roald Hoffmann for valuable discussions. K.M.L. thanks the Cornell University College of Arts and Sciences for startup funding and support from the National Science Foundation (NSF) in the form of a CAREER award (CHE-1454455). This work is based in part on research conducted at CHESS, which is supported by NSF and the National Institutes of Health/National Institute of General Medical Sciences (NIH/NIGMS) under NSF award DMR-0936374. Transmission-mode XAS was performed at SSRL, which is supported by the U.S. Department of Energy, Office of Science, Office of Basic Energy Sciences under Contract No. DE-AC02-76SF00515. The SSRL Structural Molecular Biology Program is supported by the Department of Energy's Office of Biological and Environmental Research, and by NIH/NIGMS (including P41GM103393). The content of this publication is solely the responsibility of the authors and does not necessarily represent the official views of NIGMS or NIH.

## ■ REFERENCES


(1) (a) Yale, H. L. *J. Med. Pharm. Chem.* **1958**, *1*, 121−133. (b) Purser, S.; Moore, P. R.; Swallow, S.; Gouverneur, V. *Chem. Soc. Rev.* **2008**, *37*, 320−330. (c) Müller, K.; Faeh, C.; Diederich, F. *Science* **2007**, *317*, 1881−1886.

(2) García-Monforte, M.; Martínez-Salvador, S.; Menjón, B. *Eur. J. Inorg. Chem.* **2012**, *2012*, 4945−4966.

(3) (a) Furuya, T.; Kamlet, A. S.; Ritter, T. *Nature* **2011**, *473*, 470−477. (b) Charpentier, J.; Früh, N.; Togni, A. *Chem. Rev.* **2014**, *115*, 650−682. (c) Tomashenko, O. A.; Grushin, V. V. *Chem. Rev.* **2011**, *111*, 4475−4521. (d) Liang, T.; Neumann, C. N.; Ritter, T. *Angew. Chem., Int. Ed.* **2013**, *52*, 8214−8264.

(4) (a) Lundgren, R. J.; Stradiotto, M. *Angew. Chem., Int. Ed.* **2010**, *49*, 9322−9324. (b) Ye, Y.; Sanford, M. S. *Synlett* **2012**, *23*, 2005. (c) Cho, E. J.; Senecal, T. D.; Kinzel, T.; Zhang, Y.; Watson, D. A.; Buchwald, S. L. *Science* **2010**, *328*, 1679−1681.

(5) Morimoto, H.; Tsubogo, T.; Litvinas, N. D.; Hartwig, J. F. *Angew. Chem.* **2011**, *123*, 3877−3882.

(6) Naumann, D.; Roy, T.; Tebbe, K. F.; Crump, W. *Angew. Chem., Int. Ed. Engl.* **1993**, *32*, 1482−1483.

(7) Nebra, N.; Grushin, V. V. *J. Am. Chem. Soc.* **2014**, *136*, 16998−17001.

(8) Kaupp, M.; von Schnering, H. G. *Angew. Chem., Int. Ed. Engl.* **1995**, *34*, 986−986.

(9) Snyder, J. P. *Angew. Chem., Int. Ed. Engl.* **1995**, *34*, 80−81.

(10) Jørgensen, C. K. *Coord. Chem. Rev.* **1966**, *1*, 164−178.

(11) (a) Zeng, T.; Lancaster, K. M.; Ananth, N.; Hoffmann, R. *J. Organomet. Chem.* **2015**, *792*, 6−12. (b) Aullón, G.; Alvarez, S. *Theor. Chem. Acc.* **2009**, *123*, 67−73.

(12) Alvarez, S.; Hoffmann, R.; Mealli, C. *Chem. - Eur. J.* **2009**, *15*, 8358−8373.

(13) (a) Jung, D.; Whangbo, M. H.; Alvarez, S. *Inorg. Chem.* **1990**, *29*, 2252−2255. (b) Llunell, M.; Alemany, P.; Alvarez, S.; Zhukov, V. P.; Vernes, A. *Phys. Rev. B: Condens. Matter Mater. Phys.* **1996**, *53*, 10605.




DOI: 10.1021/jacs.5b10819
*J. Am. Chem. Soc.* 2016, 138, 1922−1931

(14) (a) Zheng, C.; Hoffmann, R. *Inorg. Chem.* **1989**, *28*, 1074−1080. (b) Oana, M.; Hoffmann, R.; Abruña, H. D.; DiSalvo, F. J. *Surf. Sci.* **2005**, *574*, 1−16. (c) Grochala, W.; Hoffmann, R. *Angew. Chem., Int. Ed.* **2001**, *40*, 2742−2781. (d) Grochala, W.; Mazej, Z. *Philos. Trans. R. Soc., A* **2015**, *373*, 20140179. (e) Grochala, W.; Egdell, R. G.; Edwards, P. P.; Mazej, Z.; Žemva, B. *ChemPhysChem* **2003**, *4*, 997−1001. (f) Llunell, M.; Alvarez, S.; Alemany, P. *J. Chem. Soc., Dalton Trans.* **1998**, 1195−1200.
(15) Preiss, U.; Krossing, I. *Z. Anorg. Allg. Chem.* **2007**, *633*, 1639−1644.
(16) Romine, A. M.; Nebra, N.; Konovalov, A. I.; Martin, E.; Benet-Buchholz, J.; Grushin, V. V. *Angew. Chem., Int. Ed.* **2015**, *54*, 2745−2749.
(17) George, G. N. *EXAFSPAK*; Stanford Synchrotron Radiation Lightsource, Stanford Linear Accelerator Center; Stanford University: Stanford, CA, 2001.
(18) Finkelstein, K. D.; Lyndaker, A.; Pollock, C. J.; Krawczyk, T.; Conrad, J. *AIP Conf. Proc.*, in press.
(19) Neese, F. *WIREs Comput. Mol. Sci.* **2012**, *2*, 73−78.
(20) (a) Becke, A. D. *Phys. Rev. A: At., Mol., Opt. Phys.* **1988**, *38*, 3098−3100. (b) Perdew, J. P. *Phys. Rev. B: Condens. Matter Mater. Phys.* **1986**, *33*, 8822−8824.
(21) Stephens, P.; Devlin, F.; Chabalowski, C.; Frisch, M. J. *J. Phys. Chem.* **1994**, *98*, 11623−11627.
(22) Zhao, Y.; Truhlar, D. G. *Theor. Chem. Acc.* **2008**, *120*, 215−241.
(23) Chai, J.-D.; Head-Gordon, M. *J. Chem. Phys.* **2008**, *128*, 084106.
(24) Yanai, T.; Tew, D. P.; Handy, N. C. *Chem. Phys. Lett.* **2004**, *393*, 51−57.
(25) Neese, F.; Wennmohs, F.; Hansen, A.; Becker, U. *Chem. Phys.* **2009**, *356*, 98−109.
(26) Neese, F. *Inorg. Chim. Acta* **2002**, *337*, 181−192.
(27) (a) Weigend, F.; Ahlrichs, R. *Phys. Chem. Chem. Phys.* **2005**, *7*, 3297−3305. (b) Pantazis, D. A.; Chen, X.-Y.; Landis, C. R.; Neese, F. *J. Chem. Theory Comput.* **2008**, *4*, 908−919.
(28) van Lenthe, E.; van der Avoird, A.; Wormer, P. E. S. *J. Chem. Phys.* **1998**, *108*, 4783−4796.
(29) van Wüllen, C. *J. Chem. Phys.* **1998**, *109*, 392−399.
(30) Klamt, A.; Schüürmann, G. *J. Chem. Soc., Perkin Trans. 2* **1993**, 799−805.
(31) DeBeer George, S.; Petrenko, T.; Neese, F. *J. Phys. Chem. A* **2008**, *112*, 12936−12943.
(32) Roemelt, M.; Maganas, D.; DeBeer, S.; Neese, F. *J. Chem. Phys.* **2013**, *138*, 204101.
(33) de Groot, F. *Coord. Chem. Rev.* **2005**, *249*, 31−63.
(34) Stavitski, E.; De Groot, F. M. *Micron* **2010**, *41*, 687−694.
(35) Neese, F. *J. Chem. Phys.* **2003**, *119*, 9428−9443.
(36) Schäffer, C. E.; Jørgensen, C. K. *Mol. Phys.* **1965**, *9*, 401−412.
(37) Kropp, H.; King, A. E.; Khusniyarov, M. M.; Heinemann, F. W.; Lancaster, K. M.; DeBeer, S.; Bill, E.; Meyer, K. *J. Am. Chem. Soc.* **2012**, *134*, 15538−15544.
(38) DuBois, J. L.; Mukherjee, P.; Stack, T. D. P.; Hedman, B.; Solomon, E. I.; Hodgson, K. O. *J. Am. Chem. Soc.* **2000**, *122*, 5775−5787.
(39) Kau, L. S.; Spira-Solomon, D. J.; Penner-Hahn, J. E.; Hodgson, K. O.; Solomon, E. I. *J. Am. Chem. Soc.* **1987**, *109*, 6433−6442.
(40) Tomson, N. C.; Williams, K. D.; Dai, X.; Sproules, S.; DeBeer, S.; Warren, T. H.; Wieghardt, K. *Chem. Sci.* **2015**, *6*, 2474−2487.
(41) Hocking, R. K.; Solomon, E. I. *Struct. Bonding (Berlin, Ger.)* **2011**, *142*, 155−184.
(42) Walroth, R. C.; Uebler, J. W. H.; Lancaster, K. M. *Chem. Commun.* **2015**, *51*, 9864−9867.
(43) Neese, F.; Hedman, B.; Hodgson, K. O.; Solomon, E. I. *Inorg. Chem.* **1999**, *38*, 4854−4860.
(44) Glatzel, P.; Bergmann, U.; Gu, W.; Wang, H.; Stepanov, S.; Mandimutsira, B. S.; Riordan, C. G.; Horwitz, C. P.; Collins, T.; Cramer, S. P. *J. Am. Chem. Soc.* **2002**, *124*, 9668−9669.
(45) George, S. J.; Lowery, M. D.; Solomon, E. I.; Cramer, S. P. *J. Am. Chem. Soc.* **1993**, *115*, 2968−2969.
(46) (a) Mitzner, R.; Rehanek, J.; Kern, J.; Gul, S.; Hattne, J.; Taguchi, T.; Alonso-Mori, R.; Tran, R.; Weniger, C.; Schröder, H. *J. Phys. Chem. Lett.* **2013**, *4*, 3641−3647. (b) Kroll, T.; Hadt, R. G.; Wilson, S. A.; Lundberg, M.; Yan, J. J.; Weng, T.-C.; Sokaras, D.; Alonso-Mori, R.; Casa, D.; Upton, M. H. *J. Am. Chem. Soc.* **2014**, *136*, 18087−18099.
(47) Glatzel, P.; Yano, J.; Bergmann, U.; Visser, H.; Robblee, J. H.; Gu, W.; de Groot, F. M.; Cramer, S. P.; Yachandra, V. K. *J. Phys. Chem. Solids* **2005**, *66*, 2163−2167.
(48) Hämäläinen, K.; Siddons, D. P.; Hastings, J. B.; Berman, L. E. *Phys. Rev. Lett.* **1991**, *67*, 2850.
(49) (a) Sarangi, R.; Aboelella, N.; Fujisawa, K.; Tolman, W. B.; Hedman, B.; Hodgson, K. O.; Solomon, E. I. *J. Am. Chem. Soc.* **2006**, *128*, 8286−8296. (b) Qayyum, M. F.; Sarangi, R.; Fujisawa, K.; Stack, T. D. P.; Karlin, K. D.; Hodgson, K. O.; Hedman, B.; Solomon, E. I. *J. Am. Chem. Soc.* **2013**, *135*, 17417−17431.
(50) Szilagyi, R. K.; Metz, M.; Solomon, E. I. *J. Phys. Chem. A* **2002**, *106*, 2994−3007.
(51) Löwdin, P.-O. *Phys. Rev.* **1955**, *97*, 1474−1489.
(52) The three "c" parameters used in the DFT-ROCIS calculations were optimized for B3LYP. See ref 32.
(53) (a) Thole, B.; Van der Laan, G. *Phys. Rev. B: Condens. Matter Mater. Phys.* **1988**, *38*, 3158−3171. (b) Thole, B.; Van der Laan, G. *Phys. Rev. A: At., Mol., Opt. Phys.* **1988**, *38*, 1943−1947.
(54) Grannec, J.; Tressaud, A.; Hagenmuller, P. *J. Fluorine Chem.* **1984**, *25*, 83−90.
(55) Sinha, W.; Sommer, M. G.; Deibel, N.; Ehret, F.; Bauer, M.; Sarkar, B.; Kar, S. *Angew. Chem., Int. Ed.* **2015**, *9*, 13769−13774.


DOI: 10.1021/jacs.5b10819
*J. Am. Chem. Soc.* 2016, 138, 1922−1931